Supplementary Information

Investigating Ti-Nb alloys as supports for iridium oxide water oxidation electrocatalysts

Guangmeimei Yang[a,b], *Wei Huang*[c], *Yifeng Wang*[b], *Caiwu Liang*[a,b], *Yuxiang Zhou*[b], *Santosh Kumar*[d], *Pilar Ferrer Escorihuela*[d], *Parnia Navabpour*[e], *Giuseppe Sanzone*[e], *Trevor Ferris*[a], *Mark Turner*[f], *Sarah J. Haigh*[f], *Georg Held*[d], *Caterina Ducati*[c], *Andreas Kafizas*[a,g,†] *and Reshma R. Rao*[b,h,†]

a) Department of Chemistry, Molecular Science Research Hub, Imperial College London, White City, W12 0BZ, London, UK
b) Department of Materials, Imperial College London, South Kensington, SW7 2AZ, London, UK
c) Department of Materials Science and Metallurgy, University of Cambridge, CB3 0FS, Cambridge, UK
d) B07, Diamond Light Source, Harwell Science and Innovation Campus, Didcot OX11 0DE, UK
e) Teer Coatings Ltd, West Stone, West Stone House, Droitwich WR9 9AS, UK
f) Department of Materials, The University of Manchester, M13 9PL, Manchester, UK
g) London Centre for Nanotechnology, Imperial College London, UK
h) Grantham Institute – Climate Change and the Environment, Imperial College London, UK

[†]Corresponding authors: Dr Andreas Kafizas a.kafizas@imperial.ac.uk; Dr Reshma R. Rao reshma.rao@imperial.ac.uk

Electrochemistry workflow

A rotating disc electrode (RDE) was used in this study to examine the activities of Ti-Nb supported IrO_x. All experiments were carried out using 0.1 M $HClO_4$ as the electrolyte. Electrochemical workflow: Chronoamperometry (CA) was firstly carried out by holding the potential at 1.6 V_{RHE} for 1 hour. The current was recorded after being stabilised for activity comparison. The accelerated stress test (AST) was conducted subsequently by cycling in a potential window from 1.2 V_{RHE} to 1.7 V_{RHE} for 3,000 cycles (as shown in **Figure S1**). The electrolyte was taken out twice before and after the AST for measuring the metal dissolution.

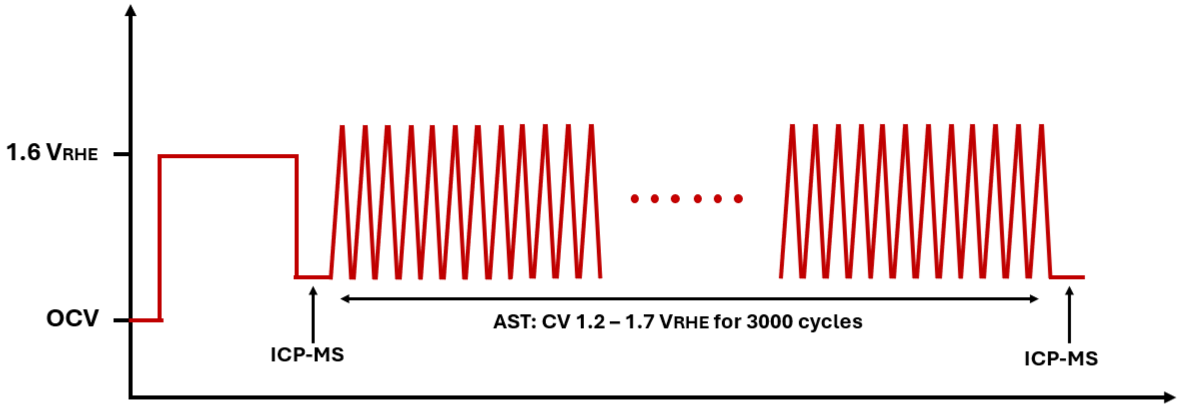

Figure S1. Demonstration of the electrochemistry workflow for the Ti-Nb samples.

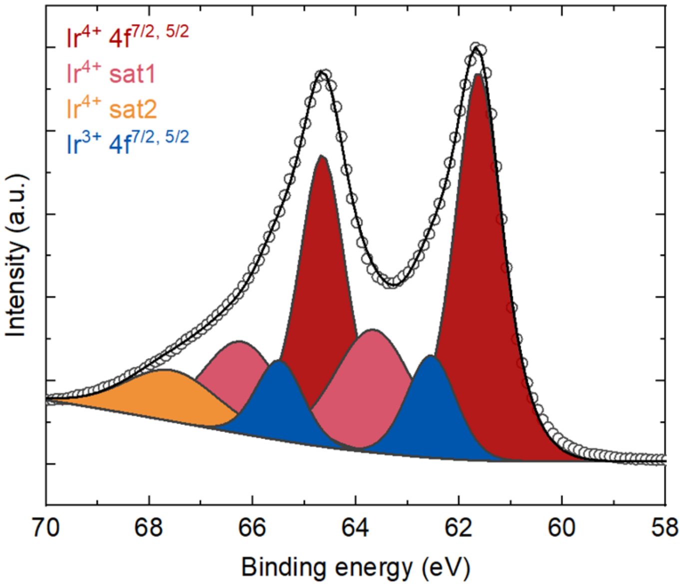

Figure S2. Ir 4f XPS spectrum with fitted components for different Ir oxidation states. The ratio between Ir^{4+} to Ir^{3+} is approximately 79% to 21%.

100 nm thick Ti-Nb thin films with varied Nb content were sputtered onto glassy carbon stubs shown in **Figure S3a** using physical vapour deposition under Ar (**Figure S3b**). **Table S1** summarises the sputter conditions.

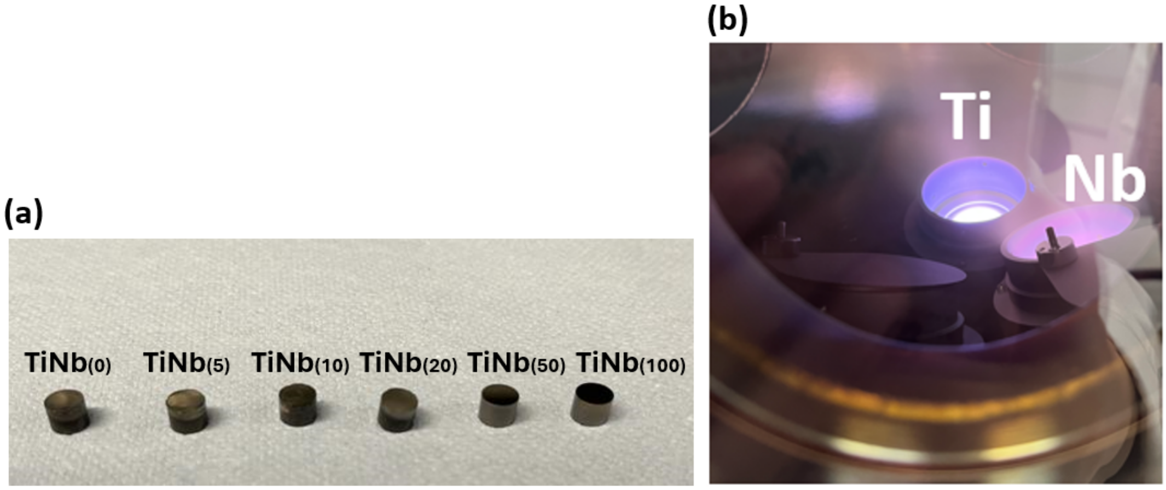

Figure S3. **(a)** Photograph of a series of $TiNb_{(x)}$ (x = 0, 5, 10, 20, 50 and 100) samples on glassy carbon substrate (RDE stub) synthesised using a sputter deposition method. **(b)** Photograph of the co-sputtering of the Ti-Nb samples in an ultra-high vacuum chamber.

Table S1. Nb content of the as-sputtered samples obtained by XPS and the parameters used for the sputter deposition (DC: direct current; RF: radio frequency)

	Nb (at%) (determined by XPS)	Ti growth rate (Å/s)	Nb growth rate (Å/s)	Coating time (s)
TiNb(0)	-	0.77 (150 W DC)	-	1299
TiNb(5)	3.2	0.77 (150 W DC)	0.045 (20 W RF)	1227

TiNb(10)	10.1	0.77 (150 W DC)	0.088 (30 W RF)	1166
TiNb(20)	15.3	0.77 (150 W DC)	0.19 (45 W RF)	1042
TiNb(50)	52.7	0.49 (100 W DC)	0.49 (100 W RF)	1020.5
TiNb(100)	-	-	0.49 (100 W RF)	2041

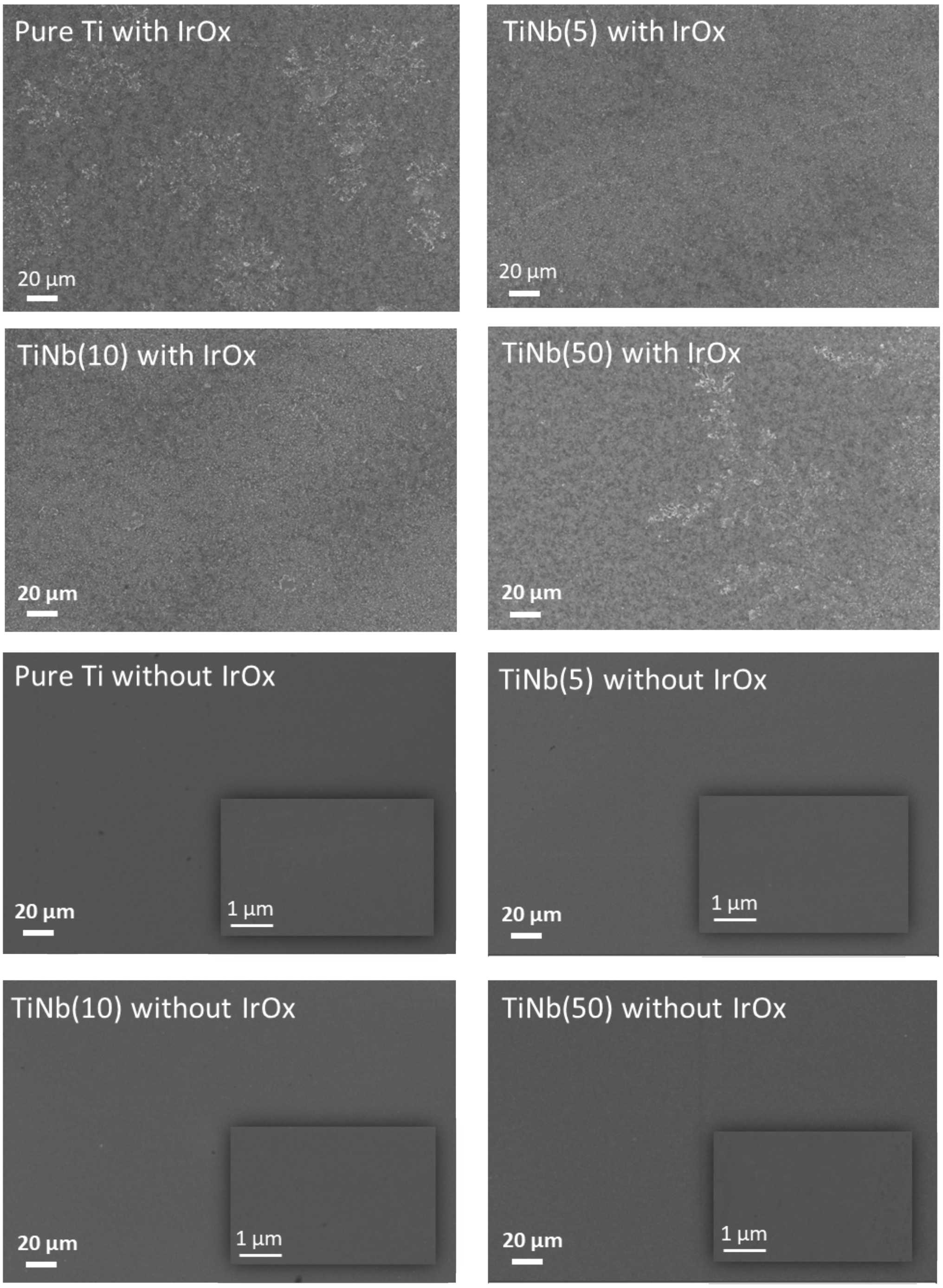

Figure S4. SEM images at 1,000 and 50,000 times magnification showing the $TiNb_{(x)}$ (x = 0, 5, 10 and 50) supports before and after deposition of the IrO_x-based ink using drop casting.

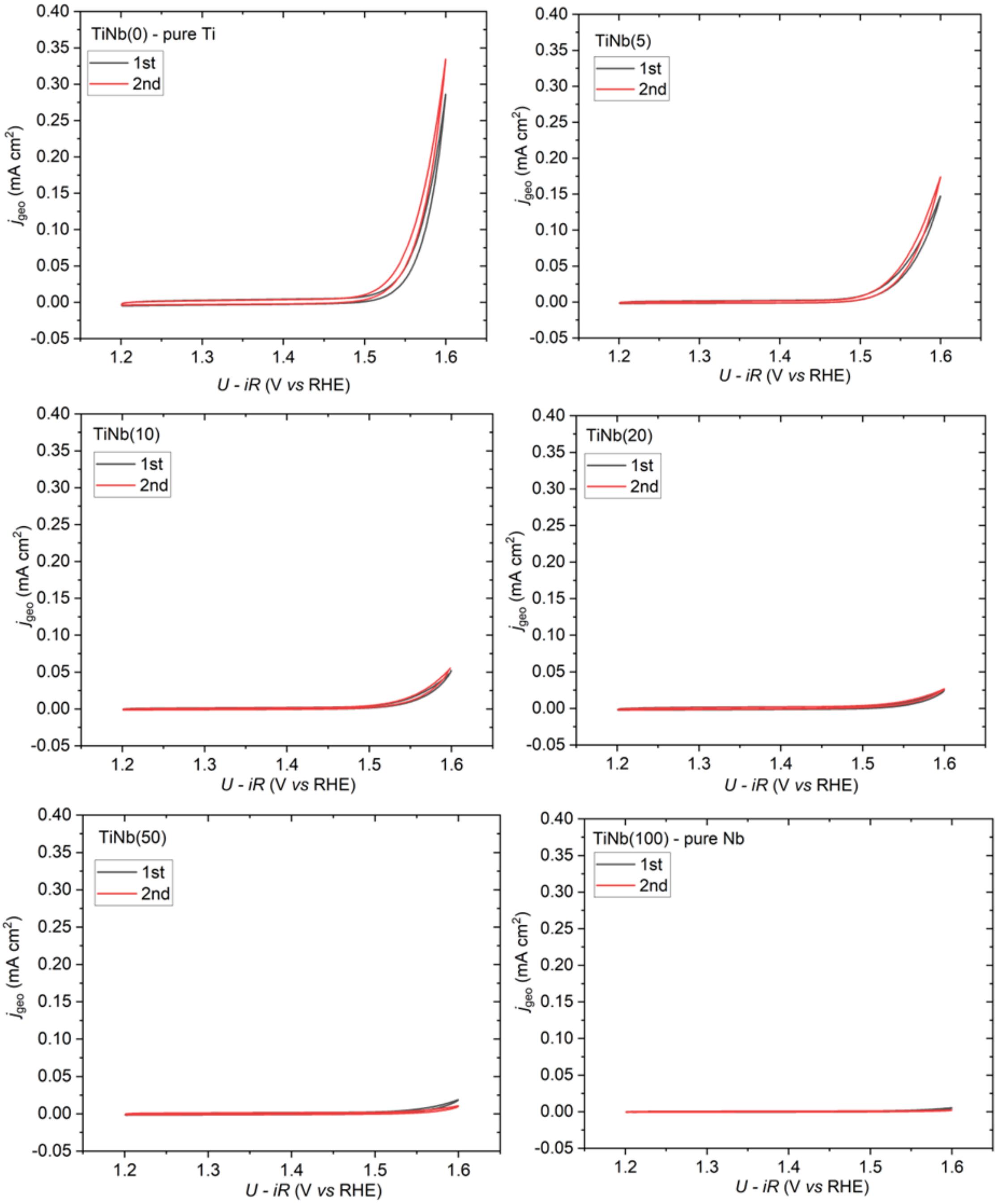

Figure S5. Cyclic Voltammograms comparing the electrochemical water oxidation activity of two independently synthesised samples that contain IrO_x supported on $TiNb_{(x)}$ (x = 0, 5, 10, 20, 50 and 100) on glassy carbon (1.2 – 1.6 V_{RHE}, 20 mV/s, 0.1 M $HClO_4$, 1600 rpm).

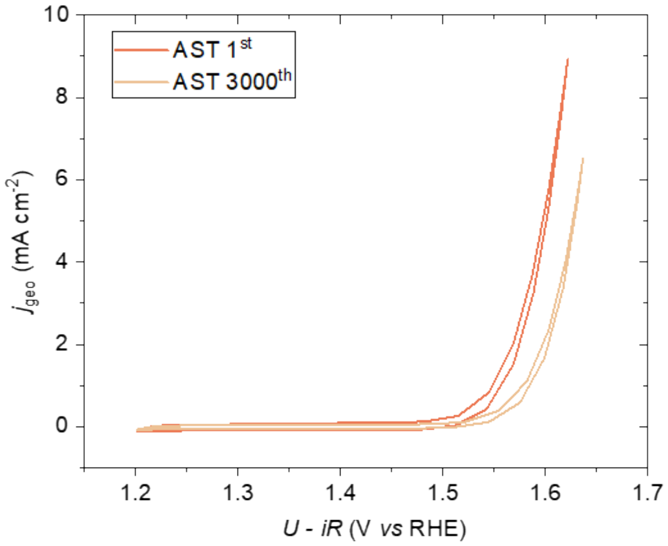

Figure S6. Initial activity of IrO_x supported on a polycrystalline gold disk and the activity after the AST, where the sample was cycled between 1.2 and 1.7 V_{RHE} at 50 mV/s in 0.1 M $HClO_4$ (pH ~1.1).

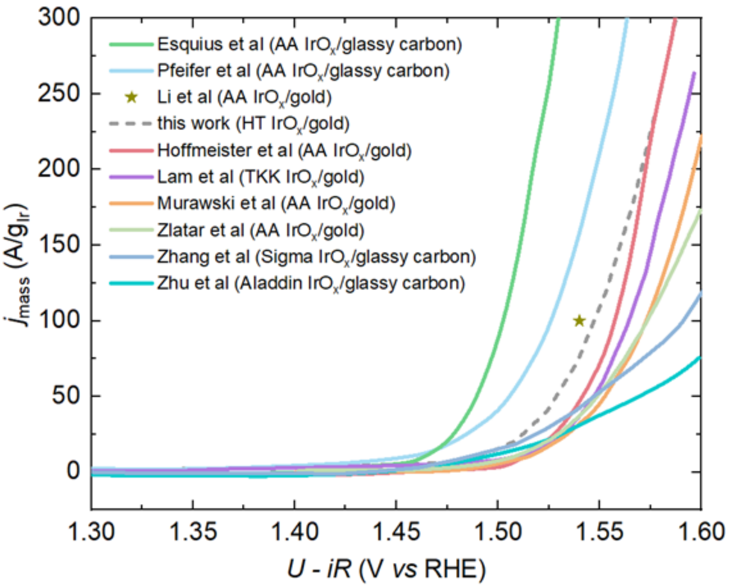

Figure S7. Comparison of the mass-normalised electrochemical water oxidation activity between this work (dotted line) and published literature (coloured lines).[1–9]

Table S2. Experimental conditions of reported IrO_x activities shown in **Figure S7**.

Refences	Substrate	Electrolyte	Type of IrOx
Esquius et al, *ACS Appl. Energy Mater.*, 2020[6]	Glassy carbon	0.1 M $HClO_4$	Alfa Aesar (AA) IrO_x
Pfeifer et al, *Phys. Chem. Chem. Phys.*, 2016[7]	Glassy carbon	0.5 M H_2SO_4	Alfa Aesar (AA) IrO_x
Li et al. *J. Am. Chem. Soc.* 2025[2]	Polycrystalline gold	0.1 M $HClO_4$	Alfa Aesar (AA) IrO_x
This work	Polycrystalline gold	0.1 M $HClO_4$	Hydrothermal IrO_x
Hoffmeister et al, *Adv. Sci.*,	Polycrystalline gold	0.1 M $HClO_4$	Alfa Aesar (AA) IrO_x

2024[8]			
Lam et al, *ACS Catal.*, 2025[5]	Polycrystalline gold	0.1 M $HClO_4$	Tanaka Kikinzoku Kogyo (TKK) IrO_x
Murawski et al, *Johnson Matthey Technol. Rev.*, 2024[3]	Polycrystalline gold	0.1 M $HClO_4$	Alfa Aesar (AA) IrO_x
Zlatar et al. *ACS Catal.*, 2023[9]	Polycrystalline gold & Glassy carbon	0.1 M $HClO_4$	Alfa Aesar (AA) IrO_x
Zhang et al. *Angew. Chem. Int. Ed.*, 2025[1]	Glassy carbon	0.5 M H_2SO_4	Sigma Aldrich IrO_2
Zhu et al, *Nat. Comm.*, 2023[4]	Glassy carbon	0.5 M H_2SO_4	Aladdin IrO_x

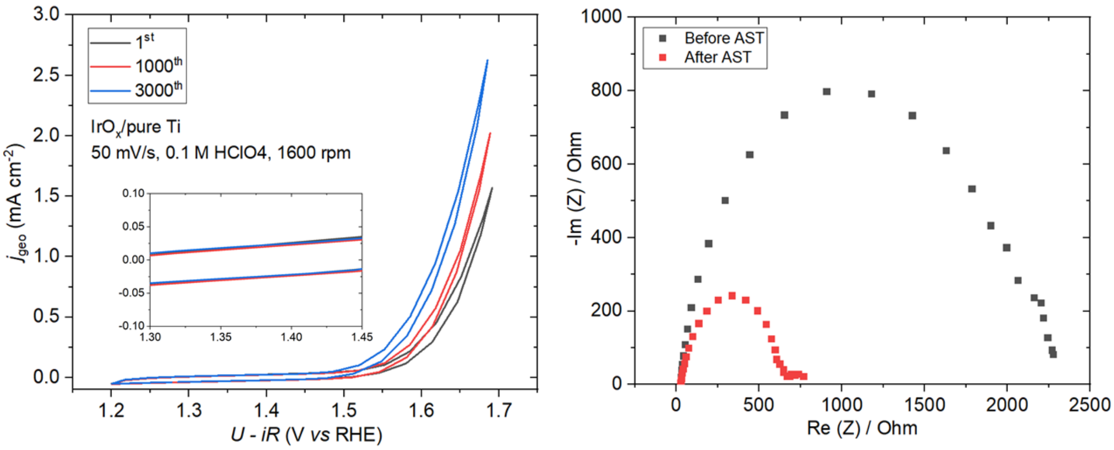

Figure S8. Cyclic voltammogram **(left)** of IrO_x supported onto TiNb(0) – pure Ti support during the AST. Cycle1, cycle 1000 and cycle 3000 are coplotted. EIS **(right)** before and after the AST.

Table S3. Calculation of Ti/Nb dissolution during AST (based on ICP-MS measurements)

NOTE: Surface area of RDE stub 0.196 cm^2; Density of Ti metal: 4.5 g/cm^3, 8.82 x 10^{-8} g/nm; Density of Nb metal: 8.6 g/cm^3, 1.68 x 10^{-7} g/nm

Nb at%	Ti dissolved (µg)	Nb dissolved (µg)	Ti dissolved (nm)	Nb dissolved (nm)
0	0.0496	-	0.56	-
5	0.045	0.0135	0.50	0.08
10	0.032	0.016	0.36	0.095
100	-	0.057		0.34

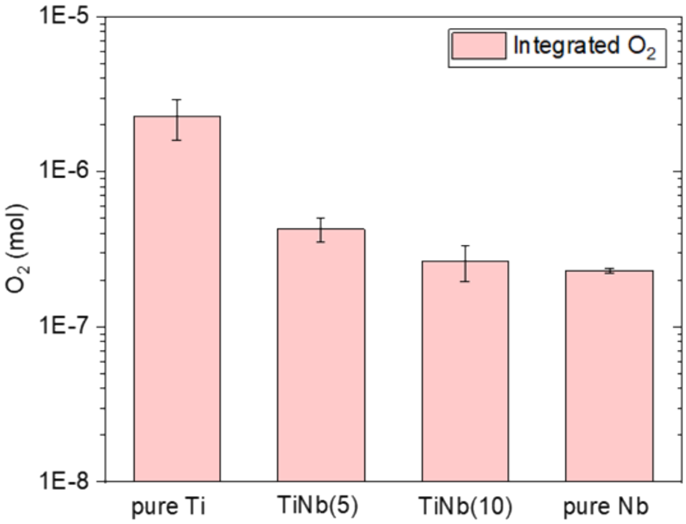

Figure S9. Integrated oxygen produced during the ASTs by integrated charges of CV scans assuming a 100% Faradaic efficiency.

Figure S10. **(a)** dissolved metals during the AST (RDE, 1.2 – 1.7 V_{RHE}, 100 mV/s, 3000 cycles, 0.1 M $HClO_4$, 1600 rpm). **(b)** S-numbers of dissolved metals (Ti, Nb and Ir) during the AST.

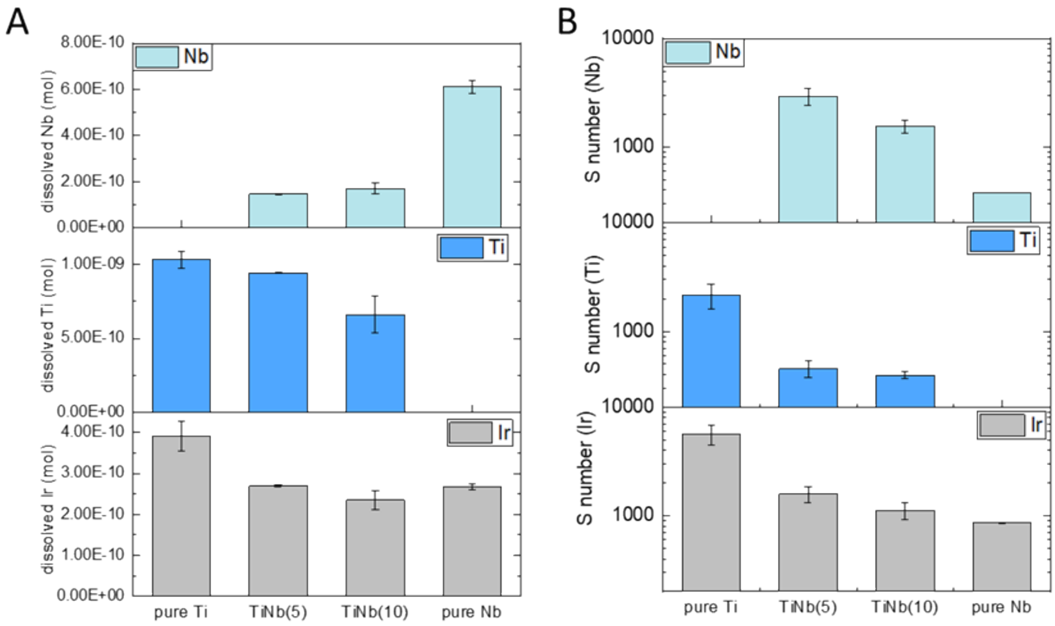

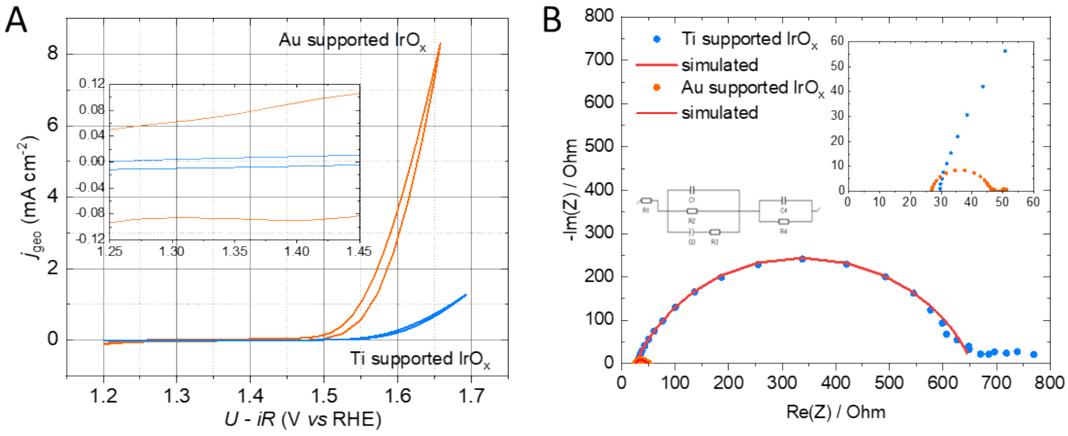

Figure S11. (a) CVs Ti supported and Au supported IrO$_x$ (RDE, 20 mV/s, 0.1 M HClO$_4$, 1600 rpm). Inset is a close-up at the non-Faradaic region. **(b)** EIS of Ti supported and Au supported IrO$_x$ at 1.6 V$_{RHE}$.

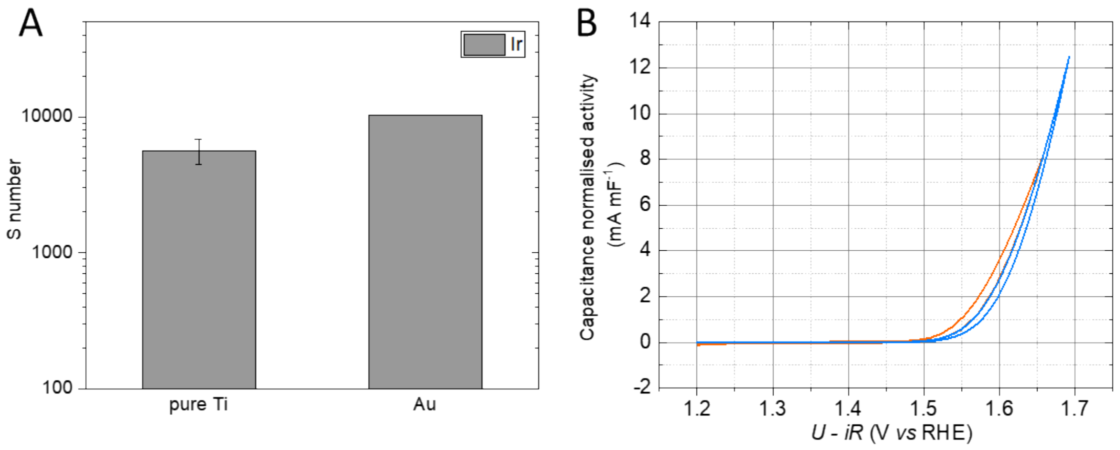

Figure S12. (a) S-numbers of Ti supported and Au supported IrO$_x$. S-numbers derived from the AST tests (RDE, 1.2 – 1.7 V$_{RHE}$, 100 mV/s, 3000 cycles, 0.1 M HClO$_4$, 1600 rpm). **(b)** Capacitance normalised activity (absolute current divided by double layer capacitance) of Ti supported and Au supported IrO$_x$.

Table S4. XPS fitting parameters (Ti 2p$_{3/2}$ and 2p$_{1/2}$). FWHM: full width half maximum

Sample name	Line shape	Binding energy (eV)	FWHM
TiNb(0) Ti^0	A(0.4,0.4,0)GL(30)	(453.8, 454.1)	(0.9,1.8)
TiNb(0) Ti^{4+}	GL(30)	(459.5,459)	(0.9,1.8)
TiNb(50) Ti^0	A(0.4,0.4,0)GL(30)	(454.1,453.8)	(0.9,1.8)
TiNb(50) Ti^{2+}	GL(30)	(456,455.5)	(0.9,1.8)
TiNb(50) Ti^{3+}	GL(30)	(457.6,457.3)	(0.9,1.8)
TiNb(50) Ti^{4+}	GL(30)	(459,459.5)	(0.9,1.8)

Table S5. XPS fitting parameters (Nb 3d$_{5/2}$ and 3d$_{3/2}$). FWHM: full width half maximum

Sample name	Line shape	Binding energy (eV)	FWHM
TiNb(0) Nb^0	A(0.4,0.4,0)GL(70)	(202.5, 202)	(0.6, 1.8)
TiNb(0) Nb^{2+}	GL(30)	(203.8, 203.2)	(0.6,1.8)

TiNb(0) Nb^{4+}	GL(30)	(206.6, 206)	(0.6,1.8)
TiNb(0) Nb^{5+}	GL(30)	(207.9, 207.3)	(0.6,1.8)
TiNb(0) Nb^{0}	A(0.4,0.4,0)GL(70)	(202.5, 202)	(0.6, 1.8)
TiNb(0) Nb^{4+}	GL(30)	(206.6, 206)	(0.6,1.8)
TiNb(0) Nb^{5+}	GL(30)	(207.9, 207.3)	(0.6,1.8)

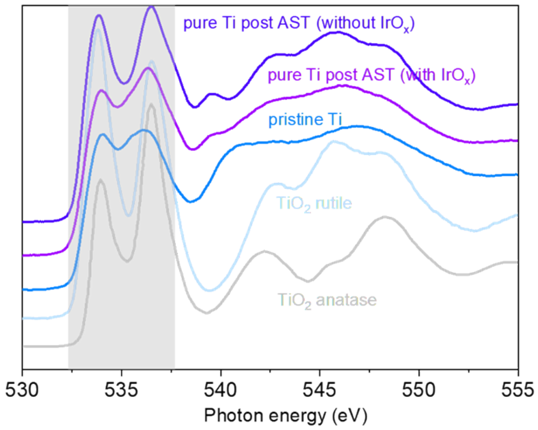

Figure S13. NEXAFS of the O K-edge of pure Ti support samples (pristine, post AST with IrO_x catalyst and without IrO_x).

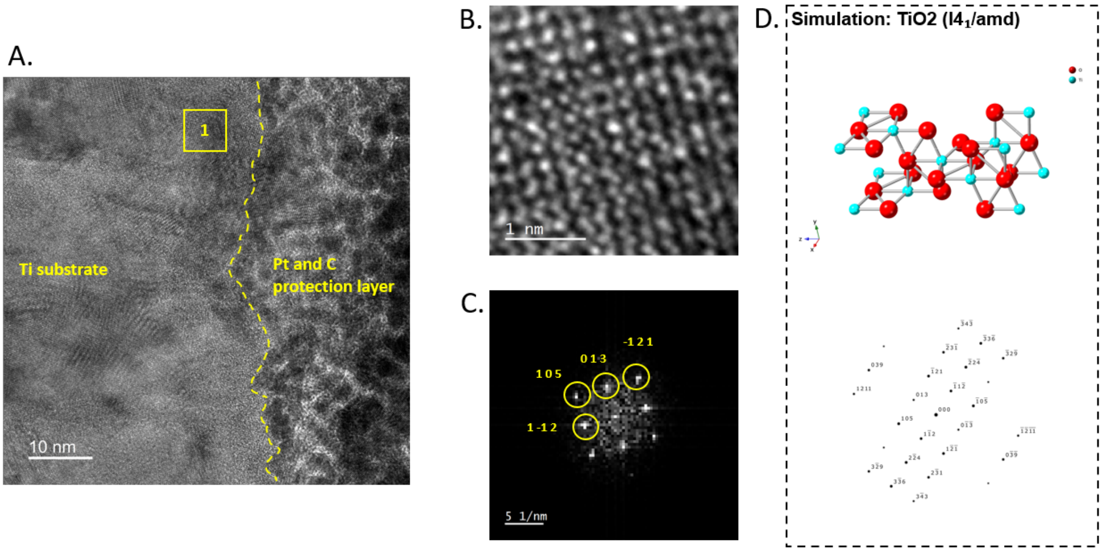

Figure S14. Transmission electron microscopy (TEM) characterisation of a focused ion beam (FIB) milled cross sectional specimen of the pure Ti after the AST tested with IrO_x. **(a)** TEM image where the left of the image is the Pt and C strap used to protect the surface of the Ti during FIB sample preparation. **(b)** Atomic lattice information from the yellow box region (1) in (a). **(c)** The Fourier transform of (b), where the spots are indexed to the anatase TiO_2 phase. **(d)** Crystalmaker atomic structure model and simulated diffraction pattern for the anatase TiO_2 phase ($I4_1/amd$).

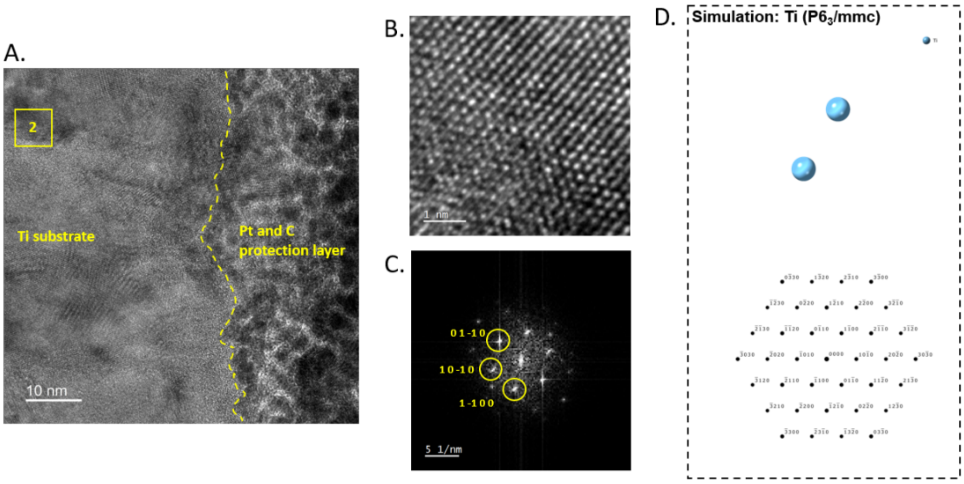

Figure S15. TEM characterisation of the same region but in the bulk shown in Figure 4 for the pure Ti after the AST tested with IrO_x. **(a)** TEM image, **(b)** Atomic lattice information from the yellow box region (2) in (a). **(c)** the Fourier transform of (b), where the spots are indexed to alpha phase metal Ti (hexagonal close packed). **(d)** Crystalmaker atomic structure model and simulated diffraction pattern for metallic alpha phase Ti ($P6_2/mmc$).

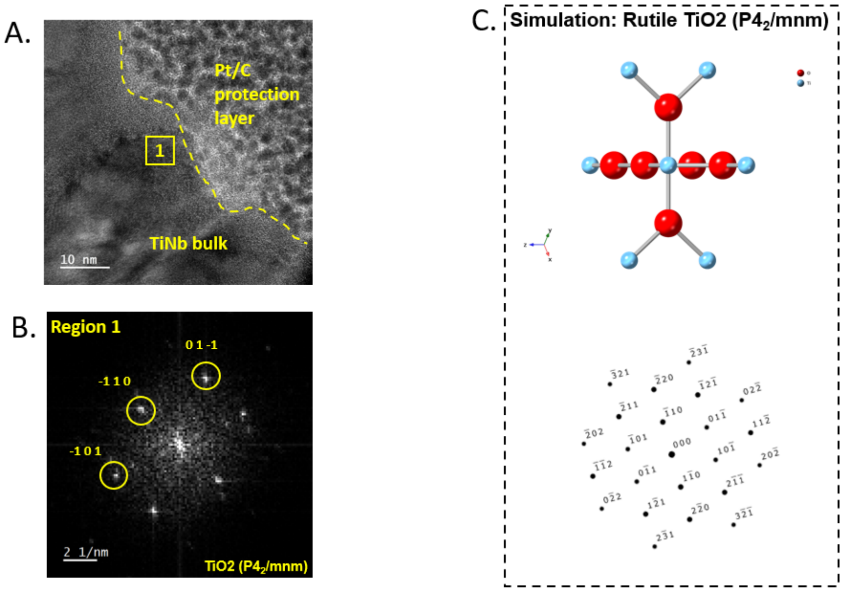

Figure S16. TEM characterisation of a FIB milled cross sectional specimen $TiNb_{(50)}$ after the AST tested with IrOx. **(a)** TEM image where the protective Pt and C coating is visible in the top right of the image. **(b)** The Fourier transform from the yellow box region (1) in (a), where the spots are indexed to rutile phase TiO_2. **(c)** Crystalmaker atomic structure model and simulated diffraction pattern for rutile TiO_2 phase ($P4_2/mnm$).

References

1 W. Zhang, C. Zhu, Y. Wen, M. Wang, Z. Lu and Y. Wang, *Angew. Chem. Int. Ed.*, DOI:10.1002/anie.202418456.

2 G. Li, A. Priyadarsini, Z. Xie, S. Kang, Y. Liu, X. Chen, S. Kattel and J. G. Chen, *J. Am. Chem. Soc.*, 2025, **147**, 7008–7016.

3 J. Murawski, S. B. Scott, R. Rao, K. Rigg, C. Zalitis, J. Stevens, J. Sharman, G. Hinds and I. E. L. Stephens, *Johnson Matthey Public Limited Company*, 2024, preprint, DOI: 10.1595/205651324X17055018154113.

4 W. Zhu, X. Song, F. Liao, H. Huang, Q. Shao, K. Feng, Y. Zhou, M. Ma, J. Wu, H. Yang, H. Yang, M. Wang, J. Shi, J. Zhong, T. Cheng, M. Shao, Y. Liu and Z. Kang, *Nat. Commun.*, DOI:10.1038/s41467-023-41036-9.

5 A. Lam, Q. Sun, Z. Polus, C. Buek, K. McCrea, I. Mahoney, L. Wegge, Z. Zeng, M. McGowan, H. Yu, F. Yang, T. Valdez, M. Hamdan and Q. Jia, *ACS Catal.*, 2025, 8414–8425.

6 J. Ruiz Esquius, D. J. Morgan, I. Spanos, D. G. Hewes, S. J. Freakley and G. J. Hutchings, *ACS Appl. Energy Mater.*, 2020, **3**, 800–809.

7 V. Pfeifer, T. E. Jones, J. J. Velasco Vélez, C. Massué, M. T. Greiner, R. Arrigo, D. Teschner, F. Girgsdies, M. Scherzer, J. Allan, M. Hashagen, G. Weinberg, S. Piccinin, M. Hävecker, A. Knop-Gericke and R. Schlögl, *Physical Chemistry Chemical Physics*, 2016, **18**, 2292–2296.

8 D. Hoffmeister, S. Finger, L. Fiedler, T. C. Ma, A. Körner, M. Zlatar, B. Fritsch, K. W. Bodnar, S. Carl, A. Götz, B. A. Zubiri, J. Will, E. Spiecker, S. Cherevko, A. T. S. Freiberg, K. J. J. Mayrhofer, S. Thiele, A. Hutzler and C. van Pham, *Advanced Science*, DOI:10.1002/advs.202402991.

9 M. Zlatar, D. Escalera-López, M. G. Rodríguez, T. Hrbek, C. Götz, R. Mary Joy, A. Savan, H. P. Tran, H. N. Nong, P. Pobedinskas, V. Briega-Martos, A. Hutzler, T. Böhm, K. Haenen, A. Ludwig, I. Khalakhan, P. Strasser and S. Cherevko, *ACS Catal.*, 2023, **13**, 15375–15392.